JCTC Journal of Chemical Theory and Computation

pubs.acs.org/JCTC Article

Self-Assembly and the Properties of Micro-Mesoporous Carbon

C. Ugwumadu,* R. Thapa, K. Nepal, A. Gautam, Y. Al-Majali, J. Trembly, and D. A. Drabold*

Cite This: https://doi.org/10.1021/acs.jctc.3c00394 Read Online

ACCESS | Metrics & More | Article Recommendations | Supporting Information

ABSTRACT: This study introduces a new approach for constructing atomistic models of nanoporous carbon by randomly distributing carbon atoms and pore volumes in a periodic box and then using empirical and *ab initio* molecular simulation tools to find the suitable energy-minimum structures. The models, consisting of 5000, 8000, 12000, and 64000 atoms, each at mass densities of 0.5, 0.75, and 1 g/cm^3, were analyzed to determine their structural characteristics and relaxed pore size distribution. Surface analysis of the pore region revealed that sp atoms exist predominantly on surfaces and act as active sites for oxygen adsorption. We also investigated the electronic and vibrational properties of the models, and localized states near the Fermi level were found to be primarily situated at sp carbon atoms through which electrical conduction may occur. Additionally, the thermal conductivity was calculated using heat flux correlations and the Green−Kubo formula, and its dependence on pore geometry and connectivity was analyzed. The behavior of the mechanical elasticity moduli (Shear, Bulk, and Young's moduli) of nanoporous carbons at the densities of interest was discussed.

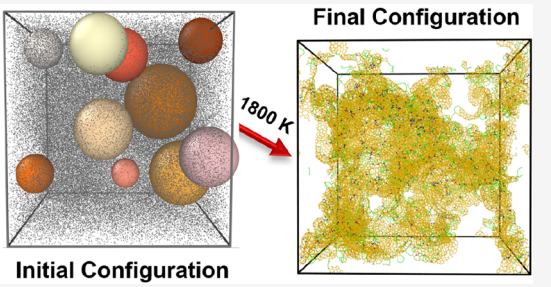

1. INTRODUCTION

Nanoporous carbon (NPC) materials are a unique class of materials known for their high surface area and intricate network of nanoscale pores. The pores can be categorized according to their size, with micropores (<20 Å), mesopores (20−500 Å), and macropores (>500 Å) being the standard IUPAC classifications.[1] However, recent research has revealed that the integration of bimodal (micro-meso, micro-macro, and meso-macro) and trimodal (micro-meso-macro and meso-meso-macro) porosity classes exists.[2,3] These tunable pore size distributions make NPC materials well-suited for a broad range of applications, including energy storage devices, catalyst supports, and gas and liquid separation.[4−6] NPCs can be synthesized by various methods, including templating, activation, and chemical vapor deposition.[7−9] Different synthetic routes lead to NPCs with distinct properties and pore morphologies, with examples including activated carbon, carbon aerogels, carbon nanotubes, and graphene-based materials.[10−14] While graphite has an interlayer spacing between its sheets of carbon atoms, its layered structure lacks well-defined nanopores and is therefore not considered an NPC material.[15,16] Similarly, multiwall fullerenes do not exhibit a porous structure and are not typically considered NPCs despite their high surface area.[17]

Although nanoporous carbon (NPC) is an important material, there is currently no widely accepted atomistic topology due to the diverse structures that can be formed by using different synthesis methods. For example, Wang and co-workers developed graphitic NPC models at varying mass densities using a highly disordered pure carbon precursor at an extremely high temperature of 9000 K, which was then graphitized at 3500 K.[18] On the other hand, Fujii[19] constructed models of NPC by creating one large spherical pore volume in the center of a dense amorphous carbon system by removing carbon atoms located in a spherical region and relaxing the configuration using the adaptive intermolecular reactive empirical bond order (AIREBO) potential.[20] In 1951, Franklin classified carbon materials into graphitizing and nongraphitizing types based on their ability to form graphite after pyrolysis at around 1200 K.[21] NPCs are typically formed from nongraphitizing carbons, which can be derived from a wide range of materials such as polymers, wood, and coconut shells. Based on Franklin's pioneering work, NPC models have been proposed as systems of strongly cross-linked graphitic bits that result in fine microporous structures. However, high-resolution transmission electron microscopy (HRTEM) observations of polyfurfuryl alcohol-derived NPCs by Kane and Foley showed that NPC produced at about 1500 K maintain a high degree of curvature and features reminiscent of fullerene.[22] These findings were further validated by HRTEM results of Harris and Tsang, even at higher temperatures between 2400 and 2600 K.[23] Their observations suggest that NPC contains pentagonal carbon rings and other nonsix-membered rings that induce curvatures,[17] thus explaining their resistance to graphitization.[21−23]

Special Issue: Computational and Theoretical Studies Focused on Self-Assembly and Molecular Organization

Received: April 6, 2023

It can be argued that the physical properties of the precursors and the conditions under which pyrolysis is carried out are more crucial than the chemical structure in determining the presence of five-membered rings in the final porous carbon structure given the wide variety of materials that can produce NPCs. Therefore, a model that can accurately describe NPCs should incorporate curved surfaces and both hexagonal and nonhexagonal rings. In an attempt to create such a model, Acharya and colleagues[24] connected fragments of graphene sheets randomly. Although this approach generated large models with nonhexagonal rings, the resulting models lacked periodicity. In this paper, atomistic models of NPC were constructed by randomly distributing carbon atoms and pore volumes in a periodic box to achieve the desired porosity. The models ranged between 5000 to 64000 atoms with a mass density between 0.5 and 1 g/cm^3. We note that it is not possible to directly simulate growth processes and offer a new approach to modeling these systems. The density-functional-theory (DFT) trained machine-learning Gaussian Approximation Potential (GAP-20)[25,26] was used for the molecular dynamics (MD) simulations. We provide a detailed description of the structure and pore topology of the model, including the observed integrated bimodal (micro-meso) porosity. We explore the electronic and vibrational signatures in NPCs such as the density of states and average thermal conductivity at room temperature. Additionally, we investigate the mechanical properties of the models in the elastic region. Our work includes elements such as the formation of NPC structures within a temperature range of 1000−1800 K that is used in the actual synthesis of NPCs, large system sizes to account for finite-size effects, and construction of NPCs from *ab initio* techniques starting with completely disordered structural configurations.

2. COMPUTATIONAL DETAILS

2.1. Model Construction. HRTEM observations show that NPC structures possess nonhexagonal rings, a high degree of curvature, and features reminiscent of fullerenes. To build models that conform to these experimental results, we implemented an algorithm that randomly creates spherical void regions in a periodic box. To ensure that the pores are not limited by the dimensions of the simulation box, we sampled the pore radii from a uniform distribution that extends maximally to half the box length. The models had 5000, 8000, 12000, and 64000 atoms, each having mass densities of 0.5, 0.75, and 1.0 g/cm^3. The porosities considered were 20, 30, and 40%. The algorithm implemented to create the initial configurations is described below:

1. Estimate the density, number of atoms, and box length.
2. Determine the desired initial porosity (Ξ_i) using eq 1, where the total number of pores N, pore volume ν_n sampled sequentially from a uniform distribution, and box volume V are known.

$$\Xi_i = \sum_{n=1}^{N} \frac{\nu_n}{V} \tag{1}$$

3. Sample the number of pores and their radii from a uniform distribution that yields the desired initial porosity.
4. Randomly place the pore centers in the simulation box, avoiding pore overlaps to maintain the porosity.
5. Randomly place the carbon atoms in the simulation box, ensuring they do not fall inside the pore volume.
6. Maintain the periodic boundary conditions throughout the process. An example of the starting model is shown in Figure 1 [left] for a 5000-atom system.

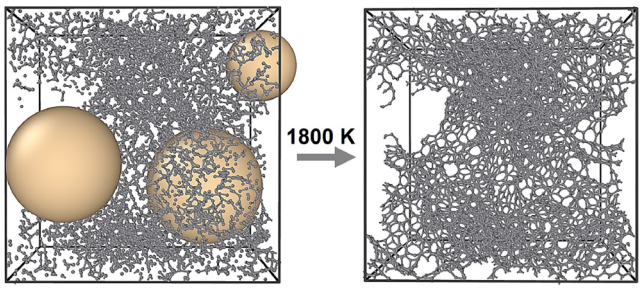

Figure 1. A 5000-atom NPC model showing the [left] initial and [right] relaxed configurations. The atoms fill some regions of the initial pore volume toward a suitable energy-minimum structure.

7. Perform NVT molecular dynamics (MD) simulation at 1800 K to obtain the final (relaxed) configuration, as shown in Figure 1 [right].

2.2. Molecular Simulation. The molecular dynamics (MD) simulation used the GAP-20 potential, developed by Rowe and colleagues,[25] which accurately represents C−C interactions. Simulations were implemented in the LAMMPS software package (Large-scale Atomic/Molecular Massively Parallel Simulator).[27] GAP-20 is an improvement on its predecessor GAP-17,[26] which has been used to predict amorphous forms of layered carbon networks, such as graphite,[15] multishell fullerenes,[17] and multiwalled nanotubes.[12] The successful use of the GAP-17 potential for amorphous graphite renewed experimental interest in exploring new routes to synthetic forms of graphite from noncrystalline carbon structures.[28,29] Unlike GAP-17, GAP-20 was additionally trained using data generated through dispersion-corrected DFT, which accounts for longer-range dispersive interactions in low-dimensional carbon structures. Consequently, it is better equipped to capture subtle differences in defect formation energies of nanostructures and to describe phonon dispersions.[25] The atomic positions and velocities of the initial models were calculated and updated in time-steps of 1 fs from a Nosé−Hoover thermostat at different temperatures between 300 and 1800 K. The energy trajectories of the systems were analyzed and accepted as a satisfactory configuration after negligible energy fluctuations were observed over an extended simulation time of at least 5 ps. Afterward, the models were allowed to find a more energetically and structurally favorable configuration by cooling to room temperature over another 10 ps. Unless otherwise specified, the analysis presented in the following discussion pertains to the 12000 atom models at T = 1800 K using GAP-20 potential in LAMMPS. This temperature conforms to the experimental procedures employed in synthesizing nanoporous carbon. The atom self-assembly process in the final structure results in the redistribution of the pore volume, leading to a statistically favorable energy minimum.

3. RESULTS AND DISCUSSIONS

3.1. Structure and Pore Size Distribution. We conducted structural analysis of the NPC models using the

https://doi.org/10.1021/acs.jctc.3c00394
J. Chem. Theory Comput. XXXX, XXX, XXX−XXX

radial distribution function (RDF), which provides insights into the spatial correlation between particles in a system. We computed the RDF for the NPC models and visually represented the results in Figure 2. Remarkably, the RDF

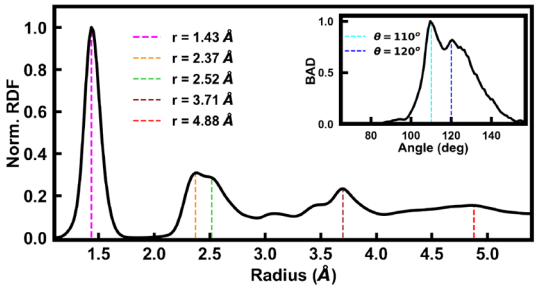

Figure 2. Radial distribution function and bond-angle distribution for the NPC models.

revealed four distinct peak positions that closely matched the experimental data obtained by Palmer and co-workers[30] for microporous carbon. These peaks were also observed in the carbon nanofoam models developed by Mathioudakis and Kelires,[31] who employed a combination of Monte Carlo and tight-binding methods.

In Figure 2, the first peak at 1.43 Å represents the nearest-neighbor distance. The peak at 2.37 Å is attributed to the presence of nonhexagonal rings within the network structure.[18] Interestingly, this peak overlaps with another peak centered at 2.52 Å, which closely aligns with the second nearest-neighbor distance, around 2.46 Å, that has been reported in other works.[18,30,31] This can be attributed to the peak at 2.37 Å caused by nonhexagonal rings. This observation was confirmed by analyzing the bond-angle distribution (BAD) in the NPC models. The BAD shown in the inset of Figure 2 indicates that angles of 110° and 120° correspond to five- and six-member rings, respectively, and are present in the NPC models. These results agree with previous HRTEM observations that reported a high proportion of nonsix-member rings, suggestive of fullerene-like curvatures in nanoporous carbon.[22,23] Furthermore, the RDF analysis revealed additional peaks at distances of 3.71 and 4.88 Å. These peaks serve as strong indications that the NPC models exhibit a coherent medium-range order,[30,31] suggesting a well-structured arrangement of particles extending beyond the nearest and second-nearest neighbors.

The `PoreSpy`[32] toolkit was used to extract the pore-network connectivity and pore-size distribution (PSD) from volumetric images of the NPC models. `PoreSpy` provides a comprehensive set of tools and functions for quantitative analysis of such images and is implemented in the `Python` programming language.[33] A model is first converted into a binary 3D matrix with voxels, where solid material is represented by one and void spaces are represented by zero. To optimize the selection process, the voxel volume of the 3D mask is set to 0.05 Å^3. The chord-length distribution and local thickness filters in `PoreSpy` were employed to estimate the PSD, which is represented by a function proportional to the integral volume of pores within an effective radius. The resulting PSD was characterized by the chord-length and pore-radius distributions, as shown in Figure 3(a) and (b), respectively. The cumulative distribution function (CDF) from the chord-length distribution provided information about the pore size and shape distribution of the NPC models, revealing that pores less than 20 Å are more probable and the probability decreases toward the box edge. The local thickness calculation revealed two peaks at around 13 and 20 Å.

Although `PoresPy` is a useful tool for analyzing pores in 3D data,[34−36] it is limited to image analysis and manipulation and does not provide 3D visualization capabilities. Figure 4 illustrates our attempt to mitigate this limitation by collapsing one dimension of the 3D binary data in various regions to visualize them as 2D slices. The resulting images in the columns of Figure 4 include the collapsed 2D images, *x*- and *y*-axes chords, and the pore thickness profile. An animation showing more of these 2D images can be found in the Supporting Information and also on our Web site.[37] The pore thickness profile reveals that although the majority of the pores fall within the micropore regime, there are regions where the pores combine and form mesopores. This indicates that the NPC models possess both micro- and mesopores. Importantly, although the initial configurations of the NPCs contained spheres with radii in the mesoporous regime, the pore distribution remained populated in the microporous regime. This suggests that the energy-optimal configuration that NPC prefers is one with chunks of interconnected micropores rather

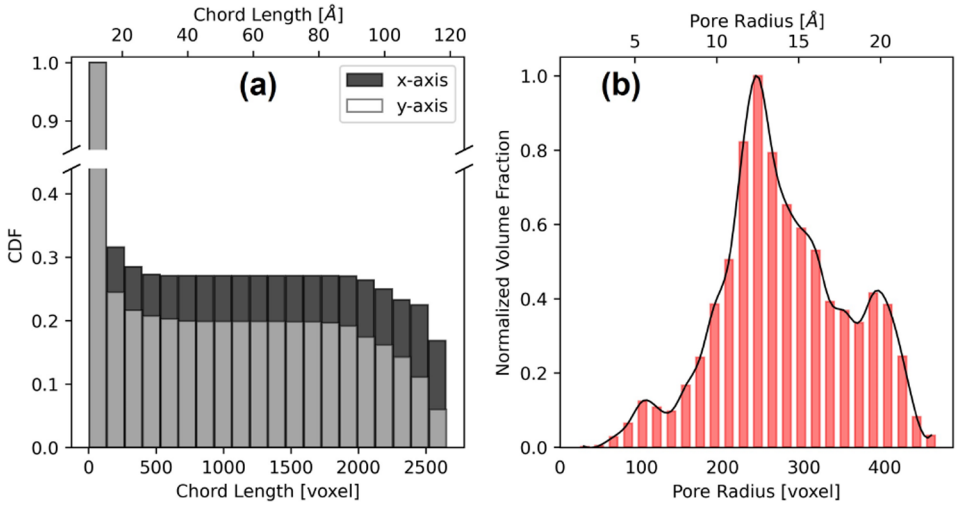

Figure 3. Cumulative distribution function (a) and pore radius histogram (b) calculated for a 64000-atom NPC model using `PoreSPy`.

https://doi.org/10.1021/acs.jctc.3c00394
J. Chem. Theory Comput. XXXX, XXX, XXX−XXX

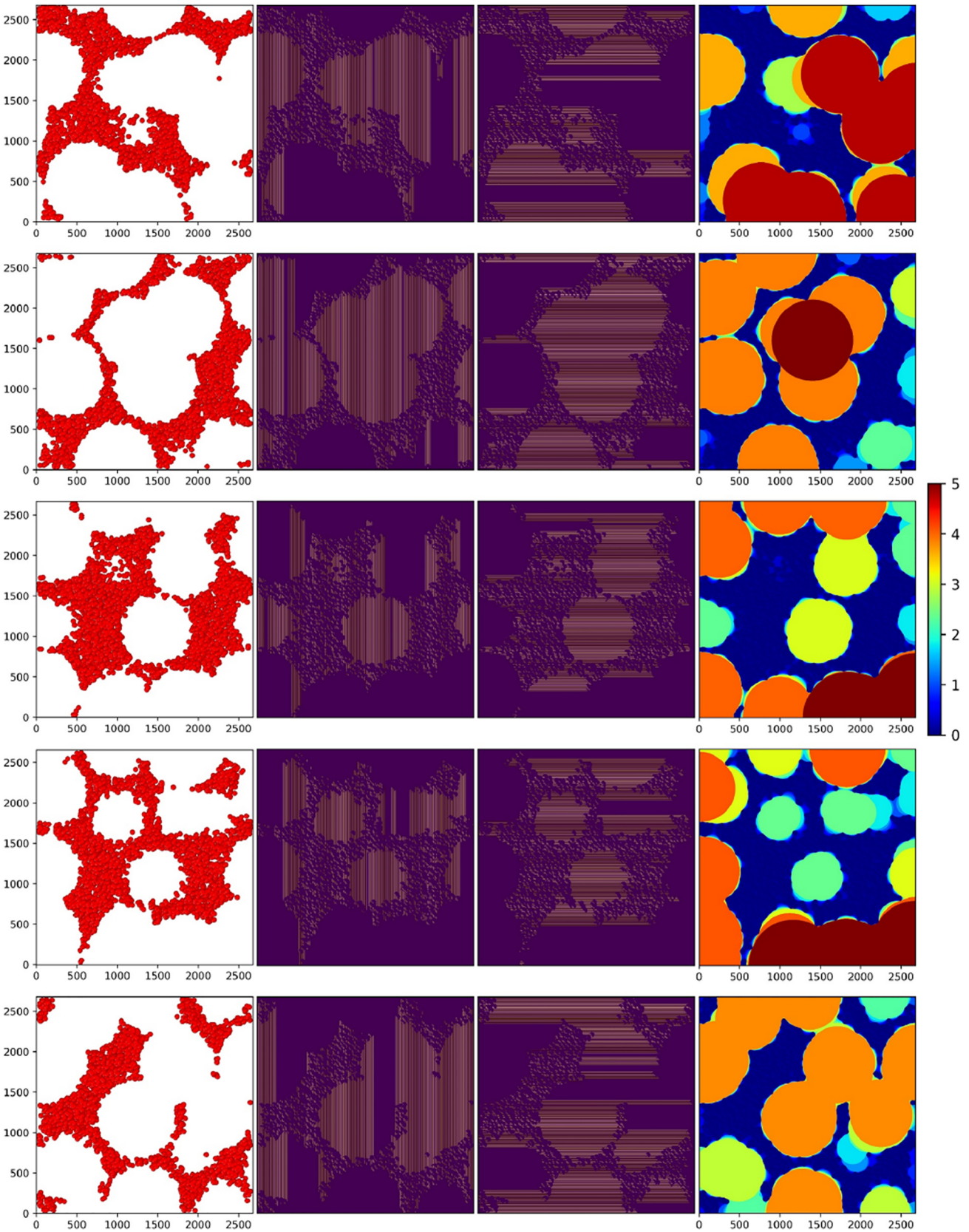

Figure 4. 2D representation of some regions in the flattened 3D binary data that produce the histograms in Figure 3. The first to the fourth column are the slices (5 Å thick), *x*- and *y*-axis chords, and pore thickness profile [$\times 10^2$ voxel].

https://doi.org/10.1021/acs.jctc.3c00394
J. Chem. Theory Comput. XXXX, XXX, XXX−XXX

than with spherical mesoporous regions. It is worth noting that the characterization of mesopores is currently limited by available tools that can explore nonsolid geometries.

3.2. Electronic, Vibrational, and Thermal Properties. The electronic properties of the models were analyzed from the electronic density of states (EDoS), and the localization of these Kohn−Sham states (ϕ) was calculated as the corresponding electronic inverse participation ratio (EIPR,) as shown in Figure 5(a), and given by the equation

$$I(\phi_n) = \frac{\sum_i |c_n^i|^4}{\left(\sum_i |c_n^i|^2\right)^2} \tag{2}$$

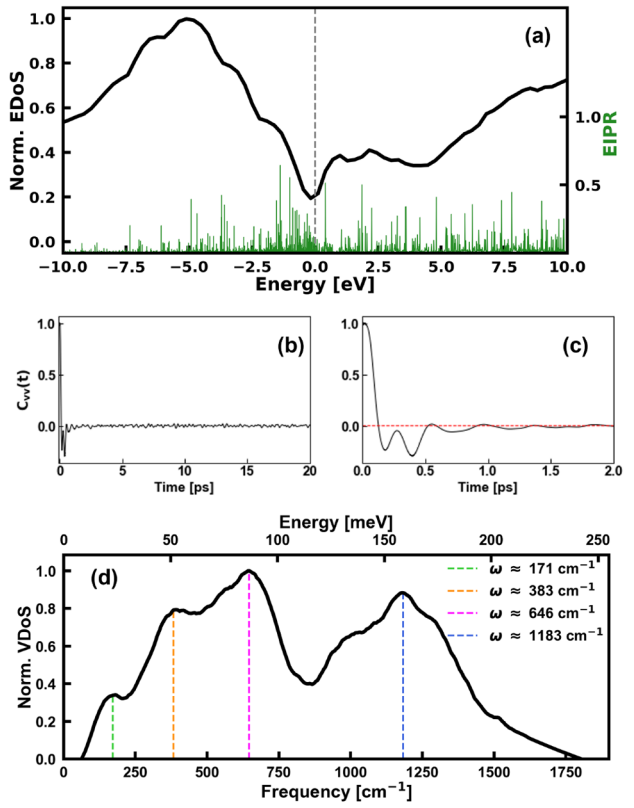

Figure 5. EDoS and VDoS calculated for a 12000-atom NPC model. (a) EDoS (black curve) and EIPR (green lines). The Fermi energy has been shifted to zero as indicated by the gray dashed line. For the VDoS calculation, the plot for the VACF is shown in (b) and (c). The Fourier transform of the VACF gives the VDoS in (d).

where c_n^i is the contribution to the eigenvector (ϕ_n) from the i^{th} atomic orbital (s and p) implemented within SIESTA (Spanish Initiative for Electronic Simulations with Thousands of Atoms).[38] For this calculation, the nonself-consistent Harris functional was implemented within the local-density approximation (LDA)[39,40] with the Perdew−Zunger parametrization.[41] Low EIPR values correspond to extended states (relatively distributed over N atoms), and high EIPR values describe localized states. Figure 5(a) shows EDoS and electronic EIPR for a 12000 atom NPC model.

The Fermi energy (E_f) in Figure 5(a) has been shifted to zero and is indicated by a gray dashed line. We note that unlike the zero-energy semimetallic gap observed in graphene and graphite, NPC exhibits many states at E_f. The EIPR shows that the states around E_f are fairly delocalized; this suggests that NPC could be more metallic than semiconducting. A similar conclusion was arrived at by Lopez and co-workers for carbide-derived nanoporous carbon.[42] Additionally, the states around the Fermi level were associated with the sp carbon atoms. The space-projected conductivity reveals that the electronic conduction pathway in low-density amorphous carbon exhibits a preference for connected sp^2 rings and sp chains in the network.[43] Thus, it can be inferred that the sp C atoms present in NPCs may play a role in the design of materials with interesting electronic properties.

The vibrational density of states (VDoS) of the NPC was calculated as the frequency spectrum determined from the Fourier transform of the velocity autocorrelation function (VACF) given as[44]

$$C_{vv}(t) = \sum_{n=1}^{N} \frac{\langle \mathbf{v}_n(t)\cdot\mathbf{v}_n(0)\rangle}{\langle \mathbf{v}_n(0)\cdot\mathbf{v}_n(0)\rangle} \tag{3}$$

Here n is the atom index, and the brackets $\langle\cdots\rangle$ indicate that an ensemble average over all atoms is taken. This ensemble average is defined by

$$\langle f(t_i)f(0)\rangle = \frac{1}{S-i+1}\sum_{s=0}^{S-1} f(t_{i+s})f(t_s) \tag{4}$$

where t_j is the time at the j^{th} step, and j = 0, 1, 2,..., S, with S representing the total number of steps in the simulation. The spectral density $g(\omega)$, which is the VDoS, is the Fourier cosine transform of the VACF ($C_{vv}(t)$) given as

$$g(\omega) = \frac{1}{T}\int_0^T C_{vv}(t)\zeta(t)\cos(\omega t)\,dt \tag{5}$$

where T is the total simulation time, and $\zeta(t)$ is the Blackman window function used to mitigate oscillations caused by finite sampling.[45] In this study, the total simulation time was set to 2 ns with time steps of 1 fs.

Figure 5(b) shows the Velocity Autocorrelation Function (VACF) for an 8000-atom model, while Figure 5(c) exhibits the expected characteristics of the VACF near t = 0, including the expected zero slope, backscattering, and asymptotic behavior. In Figure 5(d), the VDoS shares distinct features with the VDoS spectrum of nanoporous carbon models obtained by Romero and co-workers,[46] calculated using the harmonic approximation method. Specifically, both spectra terminate at around 1750 cm^{-1}, and a minimum around 110 cm^{-1} is observed in all models. However, our spectrum displays additional distinct peaks due to the inclusion of anharmonic contributions to vibrations in the implemented VACF method, which is an advantage over the VDoS obtained by Romero and co-workers.[46]

Furthermore, our spectrum exhibits similarities with the VDoS calculated for low-density amorphous carbon by Bhattarai and Drabold.[47,48] This similarity is primarily characterized by a peak in the low- and midfrequency regions at approximately 171 and 646 cm^{-1}, respectively, along with a shoulder at around 383 cm^{-1}. However, there are differences, such as the sharper peak observed in our nanoporous carbon (NPC) model at approximately 1183 cm^{-1}, whereas amorphous carbon typically displays a broader peak at around 1200 cm^{-1}. The high-frequency peak observed in NPC, consistent with the VDoS of graphite and graphene,[49] suggests the presence of local regions with ordered and disordered phases in the nanoporous carbon structure

https://doi.org/10.1021/acs.jctc.3c00394
J. Chem. Theory Comput. XXXX, XXX, XXX−XXX

We also calculated the average thermal conductivity (TC) in NPCs and evaluated the contribution of the heat flux (**J**) for each atom.[50,51] The ensemble average of the autocorrelation of **J** was then related to TC (κ) using the Green–Kubo equation[52,53] given as

$$\kappa = \frac{1}{3Vk_BT^2}\int_0^\tau \langle \mathbf{J}(0)\cdot\mathbf{J}(t)\rangle \, dt \tag{6}$$

where V, T, and k_B are the system volume, temperature, and Boltzmann's constant, respectively. The upper limit of the integral was approximated by τ (= 2 ns), which is the correlation time required for the heat current autocorrelation to decay to zero. A Nosé–Hoover thermostat[54,55] was utilized for thermalization and equilibration at T = 300 K at a fixed volume using a 1 fs time-step. Initial velocities were assigned to the atoms randomly from a Gaussian distribution. The TC exhibited slight variations within the three densities considered with a mean value of 2.64 W/(m·K) and a standard deviation of 0.07.

To explore the relationship among porosity, pore geometry, and thermal conductivity, we created six new sets of models. Each set contained 5,000 atoms, a density of 0.75 g/cm^3, and porosity levels 20%, 30%, or 40% (two models per porosity level). The models were constructed following the methodology described in Section 2, with one modification. Only one large pore was allowed, and eq 1 was adjusted accordingly:

$$\Xi_i = \frac{\nu}{V} \tag{7}$$

Here, ν represents the fixed pore volume that defines the porosity, and V denotes the volume of the simulation box. We refer to the models with multiple initial pores (connected and nonconnected) as $\mathcal{G}_1$, and the models with one large, connected pore as $\mathcal{G}_2$. It is important to highlight that, with the exception of the chosen interatomic potential and initial configurations, the construction method employed for the connected-pore models in $\mathcal{G}_2$ bears similarities to Fujii's approach,[19] which we discussed in Section 1.

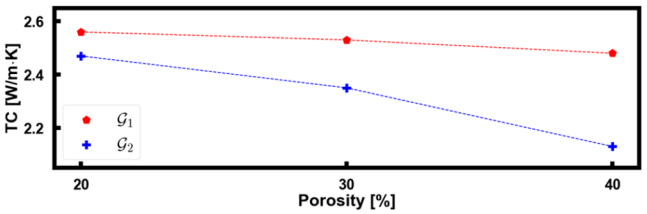

Figure 6. Influence of the pore geometry in predicting thermal conductivity.

Figure 6 presents the mean values of TC at various porosities for $\mathcal{G}_1$ and $\mathcal{G}_2$. As anticipated, the TC decreases as porosity increases. Notably, there is a substantial contrast in TC values between $\mathcal{G}_1$ and $\mathcal{G}_2$. This correlation between porosity and thermal conductivity has been previously observed by Fujii in the context of nanoporous carbon[19] and by Coquil et al. in relation to nanoporous silicon.[56] Interestingly, the TC trend obtained for $\mathcal{G}_2$ closely aligns with Fujii's findings,[19] which could be due to the connected-pore geometry inherent in both models.

These observations highlight that even at a fixed porosity the specific pore geometry plays a pivotal role in determining thermal conductivity. The contrasting behaviors exhibited by $\mathcal{G}_1$ and $\mathcal{G}_2$, characterized by connected and nonconnected pores, respectively, underscore the subtle yet crucial role of pore connectivity and geometry in influencing macroscopic properties such as TC in nanoporous materials. Hence, the accurate construction of NPC models necessitates careful consideration of pore geometry as it could exert a substantial influence on macroscopic observables beyond porosity alone.

3.3. Mechanical Properties. To investigate the mechanical properties of nanoporous carbon materials under mechanical stress in practical applications, we computed the elastic moduli, including Bulk (B), Shear (S), and Young's (Y) moduli, as a function of density. The relationship between strain (ϵ) and stress (σ) for a 3-dimensional material can be described by the following matrix equation

$$\epsilon_\alpha = C_{\alpha\beta}\sigma_\beta \tag{8}$$

where α, β = 1, 2, ..., 6, such that $C_{\alpha\beta}$ is an elastic stiffness tensor. We calculated C_{11}, C_{12}, and C_{44} for various density models at all three densities studied. By using these elastic constants, we estimated the elastic moduli as

$$B = \frac{C_{11} + 2C_{12}}{3} \quad S = C_{44} \quad Y = \frac{9SB}{3B + S} \tag{9}$$

To assess the elastic properties of nanoporous carbon under mechanical stress, we employed a strain–stress relationship using a uniform strain rate of 0.1 × 10^8 strains per second. Specifically, we applied a strain along the z-axis of the simulation box to obtain C_{11} and C_{12}, and a 4° displacement angle on a simulation box along the XY plane to obtain C_{44}. The calculated elastic constants and elastic moduli for various density models are summarized in Table 1. Our results indicate

Table 1. Elastic Constants and Elastic Moduli of Simulated Nanoporous Carbon at Different Densities

	Elastic Constant [GPa]			Elastic Moduli [GPa]		
Density [g/cm^3]	C_{11}	C_{12}	C_{44}	Y	S	B
0.50	7.42	1.04	3.11	7.13	3.11	3.17
0.75	19.35	5.10	7.11	17.20	7.11	9.85
1.00	29.55	7.23	10.02	24.48	10.02	14.67

that the elastic moduli of nanoporous carbon increase linearly with density, with Young's modulus exhibiting the steepest slope (see Figure 7). The trend in density dependence of elastic moduli is consistent with other published works.[18,57] However, we acknowledge that the elastic moduli can be

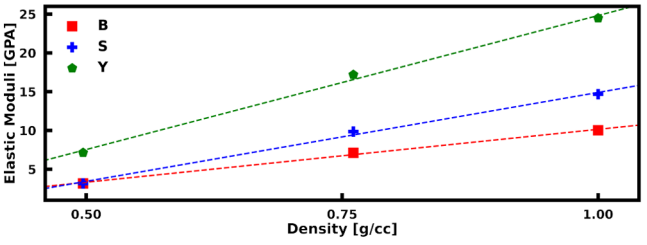

Figure 7. Elastic moduli (Bulk (B), Shear (S), and Young (Y)) as a function of density for simulated nanoporous carbons. Dashed lines are the linear fits to the calculated elastic moduli at different densities.

https://doi.org/10.1021/acs.jctc.3c00394
J. Chem. Theory Comput. XXXX, XXX, XXX–XXX

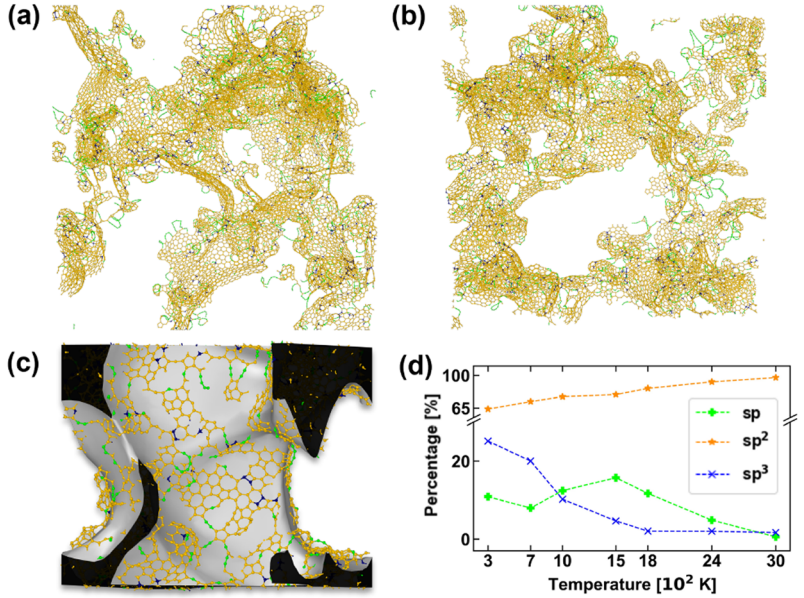

Figure 8. (a) and (b) show slices of the NPC models to portray its surface morphology, and in (c), we construct a surface to show the coordination of the carbon atom on the pore surface in NPC. The 2- (sp), 3- (sp^2), and 4-fold (sp^3) coordinated carbon atoms are represented by green, yellow, and blue colors, respectively. (d) shows the temperature dependence of the hybridization in the nanoporous carbon.

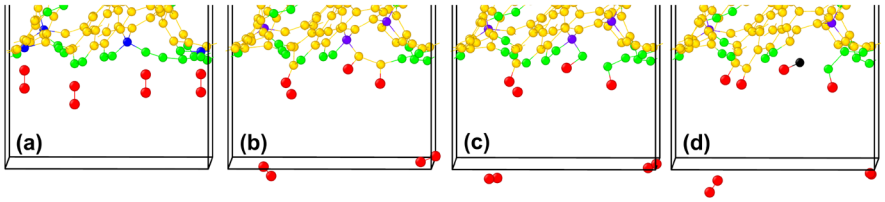

Figure 9. Mechanism of O_2 adsorption on a reconstructed surface of the NPC model at 1000 K. The O_2 (red) molecules stick to active 2-fold (sp) coordinated C sites (green) on the surface (b). This results in the breaking of the O−O bond (c) and in some cases comes off as a CO molecule (stripped C in black), as shown in (d). The 2-, 3-, and 4-fold coordinated carbon atoms are represented by green, yellow, and blue colors, respectively.

influenced by several factors, such as pore size distribution, material density, and structural defects. Nevertheless, our analysis provides a qualitative representation of the density dependence of the elastic moduli in nanoporous carbon.

4. SURFACE MORPHOLOGY AND CHEMICAL REACTIVITY

The surface morphology of NPCs plays a crucial role in determining their properties and potential applications. The high internal surface area of NPC influences its reactivity toward various substances. Surface functional groups, defects, and roughness contribute to the chemical reactivity of the material. These features can facilitate chemical reactions such as catalytic transformations or electrochemical processes. In this section, we delve into how the coordination of carbon atoms on NPC surfaces influences their surface reactivity.

Figure 8(a)−(c) presents slices of an 8000-atom NPC model, illustrating its surface morphology. The surface consists of carbon atoms with 2-fold (sp), 3-fold (sp^2), and 4-fold (sp^3) coordination, represented by green, yellow, and blue colors, respectively. Figure 8(c) reveals that the 2-fold coordinated carbon atoms are predominantly located on the surface and are well-known to act as reactive sites.[58] The distribution of carbon coordination in NPCs can vary, depending on the preparation temperature. Figure 8 illustrates the temperature dependence of carbon hybridization in NPCs. Our results demonstrate a gradual increase (decrease) in the percentage of sp^2 (sp^3) hybridized atoms as the temperature rises. Notably, the fraction of sp-hybridized carbon atoms reaches its peak around 1500 K.

The skeletal framework of NPC is predominantly composed of carbon atoms. Nevertheless, its elemental composition is not limited to carbon and may comprise hydrogen, oxygen, and other species, as well. Furthermore, depending on the precursor and the method of preparation, NPC may also contain other heteroatoms that can react with the unsaturated carbon atoms present in the material. The surface reactivity of NPC toward oxygen, which depends upon unsaturated bonds on its surface, plays a crucial role in its potential applications in fields like catalysis or gas separation. It also explains (in part) the adsorption of water molecules in the mesopores of vitreous carbon foams made from precursors like furfuryl alcohol or phenolic resin.[59,60]

Ideally, investigating the oxygen adsorption mechanism on the NPC surface would involve placing the oxygen molecules directly within the pore region in the NPC model. However, this approach is computationally expensive due to the large size and complexity of the NPC structure. As an alternative, we employed the method developed by Bhattarai and Drabold[47] to analyze the oxygen adsorption on surface models of

https://doi.org/10.1021/acs.jctc.3c00394
J. Chem. Theory Comput. XXXX, XXX, XXX−XXX

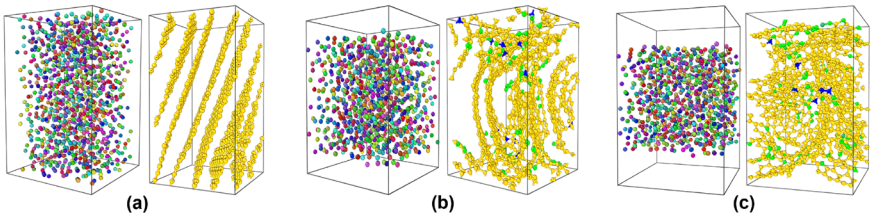

Figure 10. Dependence of pore characterization on density and thermal preparation. All the figures were obtained at 3000 K using a 1200-atom model, and we maintain the density at (a) 2.4 g/cm^3, (b) 1.8 g/cm^3, and (c) 1.5 g/cm^3. The starting configuration in (b) and (c) involves adding 6 and 12 Å vacuum, respectively, in the *z*-axis of the model in (a). The left-hand figures, in multicolors, are the starting configurations. The right-hand ones represent the final models. The sp, sp^2, and sp^3 configurations are represented by green, yellow, and blue colors, respectively.

amorphous carbon. The rationale behind using surface models of amorphous carbon is that they provide numerous representative sites that are likely to occur on the surfaces of NPCs, as illustrated in Figure 8. Although amorphous carbon lacks the pore structure present in NPCs, it shares a similar chemical environment, allowing us to gain insights into some of the locality-dependent chemistry of NPCs.[19,61,62]

We constructed an amorphous carbon model with a density of 0.75 g/cm^3. The surface slab was created by increasing the *z*-axis by 15 Å. The slab was relaxed using a conjugate gradient (CG) algorithm with a force tolerance of 0.02 eV/Å, employing the plane-wave DFT software package, VASP (Vienna Ab initio Simulation Package), in the generalized gradient approximation (GGA) of Perdew−Burke−Ernzerhof (PBE).[63,64] The preference for employing VASP (with plane-wave DFT) over GAP-20 is because GAP-20 is specifically trained for pure carbon systems, whereas VASP offers more versatility for studying a wider range of materials and systems.

Figure 9 depicts the adsorption of the O_2 on the reactive NPC surface. Oxygen molecules (in red) were randomly placed at a distance >2 Å from the nearest carbon atom on the surface. In Figure 9, the sp, sp^2, and sp^3 configurations are represented by green, yellow, and blue colors, respectively. Subsequent NVT simulation results of the resulting surface/oxygen model, heated at 1000 K, indicated that the sp atoms on the surface are the most reactive with oxygen, while the sp^2 and sp^3 C atoms do not participate in the adsorption reaction. The oxygen atoms bond to the sp carbon, and in some cases, the carbon atom is stripped from the surface by oxygen as CO or CO_2 (refer to Figure 9(d); the stripped C atom is colored in black).

It should be noted, however, that the atomic coordination of NPCs is dependent not only on the processing temperature but also on the initial assumptions made for the model. To illustrate this, we created three 1200-atom models, as shown in Figure 10, at 3000 K with densities of (a) 2.4 g/cm^3, (b) 1.8 g/cm^3, and (c) 1.5 g/cm^3. In configurations (b) and (c), 6 and 12 Å vacuum, respectively, were added to the *z*-axis of the model in Figure 10(a). The left-hand figures in Figure 10 (in multicolors) represent the initial configurations, while the right-hand figures depict the final models obtained as discussed in Section 2.2. Interestingly, Figure 10(b) and (c) suggest a preference for low densities for NPC formation, in contrast to amorphous graphite that forms at high densities (see Figure 10(a)).

5. CONCLUSIONS

In this study, we developed models of nanoporous carbon with varying porosities at different temperatures by randomly distributing carbon atoms and pore volumes in a periodic box. We used three system sizes of 5000, 8000, 12000, and 64000 atoms with mass densities of 0.5, 0.75, and 1 g/cm^3. The radial distribution function demonstrated behavior consistent with amorphous carbon, and bond-angle analysis confirmed a high presence of nonhexagonal rings. Pore size distribution analysis showed that micropores dominated but tended to overlap rather than form a single mesopore, as suggested by a 2D representation of the 3D binary image. Surface analysis of the pore region revealed that sp atoms remained mostly on the surfaces and served as active sites for oxygen adsorption. Furthermore, the electronic density of states analysis indicated that a few localized states were primarily situated at these sp carbon atoms near the Fermi level. The vibrational density of states calculated from the velocity autocorrelation at 300 K displayed peaks characteristic of both crystalline and amorphous phases. The mean thermal conductivity using the heat flux and Green−Kubo formula was 2.64 W/(m·K) with a standard deviation of 0.07. Additionally, it was observed that beyond the level of porosity, the geometry and connectivity of the pore volumes significantly influence macroscopic observables such as thermal conductivity. Finally, we investigated the mechanical elasticity of nanoporous carbons and observed a linear increase in elastic moduli with increasing densities, with Young's modulus being the most sensitive to these changes.

■ ASSOCIATED CONTENT

Supporting Information

The Supporting Information is available free of charge at https://pubs.acs.org/doi/10.1021/acs.jctc.3c00394.

Animation showing pore distribution in nanoporous carbon in 2D. The animation was created by Ms. Rawan Nowier (Physics Dept., Ohio University) (MP4)

■ AUTHOR INFORMATION

Corresponding Authors

C. Ugwumadu − *Department of Physics and Astronomy, Nanoscale and Quantum Phenomena Institute (NQPI), Ohio University, Athens, Ohio 45701, United States;* orcid.org/0000-0001-9920-7594; Email: cu884120@ohio.edu

D. A. Drabold − *Department of Physics and Astronomy, Nanoscale and Quantum Phenomena Institute (NQPI), Ohio University, Athens, Ohio 45701, United States;* Email: drabold@ohio.edu

Authors

R. Thapa − *Department of Physics and Astronomy, Nanoscale and Quantum Phenomena Institute (NQPI), Ohio University, Athens, Ohio 45701, United States*

https://doi.org/10.1021/acs.jctc.3c00394
J. Chem. Theory Comput. XXXX, XXX, XXX−XXX

K. Nepal − *Department of Physics and Astronomy, Nanoscale and Quantum Phenomena Institute (NQPI), Ohio University, Athens, Ohio 45701, United States*
A. Gautam − *Department of Physics and Astronomy, Nanoscale and Quantum Phenomena Institute (NQPI), Ohio University, Athens, Ohio 45701, United States*
Y. Al-Majali − *Department of Mechanical Engineering, Institute for Sustainable Energy and the Environment (ISEE), Ohio University, Athens, Ohio 45701, United States*
J. Trembly − *Department of Mechanical Engineering, Institute for Sustainable Energy and the Environment (ISEE), Ohio University, Athens, Ohio 45701, United States;* orcid.org/0000-0002-9851-2914

Complete contact information is available at: https://pubs.acs.org/10.1021/acs.jctc.3c00394

Notes

The authors declare no competing financial interest.

■ ACKNOWLEDGMENTS

D.A.D. and C.U. express their sincere appreciation to Dr. Rudolph Olson III (CONSOL Innovations) and Prof. H. E Castillo (Physics Dept., Ohio University) for their valuable insights and contributions during the course of this work, which greatly improved the quality of the research. C.U. also thanks Ms. Rawan Nowier (Physics Dept., Ohio University) for her assistance in creating the pore distribution animations used in this work. This work used computational resources at Pittsburgh Supercomputing Center (Bridges-2 Regular Memory) through allocation DMR-190008P from Extreme Science and Engineering Discovery Environment (XSEDE) and allocation phy230007p from the Advanced Cyberinfrastructure Coordination Ecosystem: Services & Support (ACCESS) programs. Both are supported by National Science Foundation grants: ACI-1548562 (for XSEDE) and 2138259, 2138286, 2138307, 2137603, and 2138296 (for ACCESS).

■ REFERENCES

(1) Thommes, M.; Kaneko, K.; Neimark, A. V.; Olivier, J. P.; Rodriguez-Reinoso, F.; Rouquerol, J.; Sing, K. S. Physisorption of gases, with special reference to the evaluation of surface area and pore size distribution (IUPAC Technical Report). *Pure and applied chemistry* **2015**, *87*, 1051−1069.
(2) Su, B.-L.; Sanchez, C.; Yang, X.-Y. *Hierarchically structured porous materials: from nanoscience to catalysis, separation, optics, energy, and life science*; John Wiley & Sons: 2012.
(3) Bae, W.-G.; Kim, H. N.; Kim, D.; Park, S.-H.; Jeong, H. E.; Suh, K.-Y. 25th anniversary article: scalable multiscale patterned structures inspired by nature: the role of hierarchy. *Adv. Mater.* **2014**, *26*, 675−700.
(4) Ramesh, A.; Jeyavelan, M.; Rajju Balan, J. A.; Srivastava, O.; Leo Hudson, M. S. Supercapacitor and room temperature H, CO2 and CH4 gas storage characteristics of commercial nanoporous activated carbon. *J. Phys. Chem. Solids* **2021**, *152*, 109969.
(5) Sun, M.-H.; Huang, S.-Z.; Chen, L.-H.; Li, Y.; Yang, X.-Y.; Yuan, Z.-Y.; Su, B.-L. Applications of hierarchically structured porous materials from energy storage and conversion, catalysis, photocatalysis, adsorption, separation, and sensing to biomedicine. *Chem. Soc. Rev.* **2016**, *45*, 3479−3563.
(6) Pal, A.; Uddin, K.; Saha, B. B.; Thu, K.; Kil, H.-S.; Yoon, S.-H.; Miyawaki, J. A benchmark for CO2 uptake onto newly synthesized biomass-derived activated carbons. *Applied Energy* **2020**, *264*, 114720.
(7) Malgras, V.; Tang, J.; Wang, J.; Kim, J.; Torad, N. L.; Dutta, S.; Ariga, K.; Hossain, M.; Shahriar, A.; Yamauchi, Y.; et al. Fabrication of nanoporous carbon materials with hard-and soft-templating approaches: A review. *J. Nanosci. Nanotechnol.* **2019**, *19*, 3673−3685.
(8) Mestre, A. S.; Carvalho, A. P. Nanoporous carbon synthesis: An old story with exciting new Chapters. *Porosity*; Ghrib, T., Ed.; IntechOpen: London, UK, 2018; pp 37−68.
(9) Manawi, Y. M.; Samara, A.; Al-Ansari, T.; Atieh, M. A. A review of carbon nanomaterials' synthesis via the chemical vapor deposition (CVD) method. *Materials* **2018**, *11*, 822.
(10) Heidarinejad, Z.; Dehghani, M. H.; Heidari, M.; Javedan, G.; Ali, I.; Sillanpää, M. Methods for preparation and activation of activated carbon: a review. *Environmental Chemistry Letters* **2020**, *18*, 393−415.
(11) Lee, J.-H.; Park, S.-J. Recent advances in preparations and applications of carbon aerogels: A review. *Carbon* **2020**, *163*, 1−18.
(12) Ugwumadu, C.; Thapa, R.; Al-Majali, Y.; Trembly, J.; Drabold, D. A. Formation of Amorphous Carbon Multi-Walled Nanotubes from Random Initial Configurations. *physica status solidi (b)* **2023**, *260*, 2200527.
(13) Kapko, V.; Drabold, D. A.; Thorpe, M. F. Electronic structure of a realistic model of amorphous graphene. *physica status solidi (b)* **2010**, *247*, 1197−1200.
(14) Yuan, W.; Chen, J.; Shi, G. Nanoporous graphene materials. *Mater. Today* **2014**, *17*, 77−85.
(15) Thapa, R.; Ugwumadu, C.; Nepal, K.; Trembly, J.; Drabold, D. A. Ab Initio Simulation of Amorphous Graphite. *Phys. Rev. Lett.* **2022**, *128*, 236402.
(16) Ugwumadu, C.; Thapa, R.; Nepal, K.; Drabold, D. A. Atomistic nature of amorphous graphite. *European Journal of Glass Science and Technology Part B* **2023**, *64*, 16−22.
(17) Ugwumadu, C.; Nepal, K.; Thapa, R.; Lee, Y.; Al Majali, Y.; Trembly, J.; Drabold, D. Simulation of multi-shell fullerenes using Machine-Learning Gaussian Approximation Potential. *Carbon Trends* **2023**, *10*, 100239.
(18) Wang, Y.; Fan, Z.; Qian, P.; Ala-Nissila, T.; Caro, M. A. Structure and pore size distribution in nanoporous carbon. *Chem. Mater.* **2022**, *34*, 617−628.
(19) Fujii, A. M. K. *Effect of nanoporosity on the thermal conductivity of amorphous carbon*; University of California, Los Angeles, 2014.
(20) Stuart, S. J.; Tutein, A. B.; Harrison, J. A. A reactive potential for hydrocarbons with intermolecular interactions. *J. Chem. Phys.* **2000**, *112*, 6472−6486.
(21) Franklin, R. E. Crystallite growth in graphitizing and non-graphitizing carbons. *Proceedings of the Royal Society of London. Series A. Mathematical and Physical Sciences* **1951**, *209*, 196−218.
(22) Kane, M. S.; Foley, H. C. Local microstructural organization in carbogenic molecular sieves. *MRS Online Proceedings Library (OPL)* **1996**, *431*, 9.
(23) Harris, P. J.; Tsang, S. C. High-resolution electron microscopy studies of non-graphitizing carbons. *Philosophical Magazine A* **1997**, *76*, 667−677.
(24) Acharya, M.; Strano, M. S.; Mathews, J. P.; Billinge, S. J.; Petkov, V.; Subramoney, S.; Foley, H. C. Simulation of nanoporous carbons: a chemically constrained structure. *Philosophical Magazine B* **1999**, *79*, 1499−1518.
(25) Rowe, P.; Deringer, V. L.; Gasparotto, P.; Csányi, G.; Michaelides, A. An accurate and transferable machine learning potential for carbon. *J. Chem. Phys.* **2020**, *153*, 034702.
(26) Deringer, V. L.; Csányi, G. Machine learning based interatomic potential for amorphous carbon. *Phys. Rev. B* **2017**, *95*, 094203.
(27) Thompson, A. P.; Aktulga, H. M.; Berger, R.; Bolintineanu, D. S.; Brown, W. M.; Crozier, P. S.; in 't Veld, P. J.; Kohlmeyer, A.; Moore, S. G.; Nguyen, T. D.; Shan, R.; Stevens, M. J.; Tranchida, J.; Trott, C.; Plimpton, S. J. LAMMPS - a flexible simulation tool for particle-based materials modeling at the atomic, meso, and continuum scales. *Comput. Phys. Commun.* **2022**, *271*, 108171.
(28) Chiacchia, K. Ohio University Simulations on PSC Supercomputer Transform Coal-Like Material to Amorphous Graphite and Nanotubes. www.psc.edu/ohio-university-simulations-on-psc-

supercomputer-transform-coal-like-material-to-amorphous-graphite-and-nanotubes (accessed 2023-03-27).
(29) materialstoday. Amorphous graphite adds new layer to carbon materials. www.materialstoday.com/carbon/news/amorphous-graphite-layer-carbon-materials/ (accessed 2023-05-20).
(30) Palmer, J.; Jain, S.; Gubbins, K.; Cohaut, N.; Fischer, J.; Dash, R.; Gogotsi, Y. Hybrid reverse monte carlo simulations of microporous carbons. *Characterisation of porous solids viii: Proceedings of the 8th International Symposium on the Characterisation of Porous Solids*; Royal Soc. Chemistry: Cambridge, 2009; pp 56−63.
(31) Mathioudakis, C.; Kelires, P. C. Atomistic simulations of low-density nanoporous materials: carbon nanofoams. *Phys. Rev. B* **2013**, *87*, 195408.
(32) Gostick, J. T.; Khan, Z. A.; Tranter, T. G.; Kok, M. D.; Agnaou, M.; Sadeghi, M.; Jervis, R. PoreSpy: A python toolkit for quantitative analysis of porous media images. *Journal of Open Source Software* **2019**, *4*, 1296.
(33) Van Rossum, G.; Drake, F. L., Jr. *Python tutorial*; Centrum voor Wiskunde en Informatica: Amsterdam, The Netherlands, 1995; Vol. *620*.
(34) Ávila, J.; Pagalo, J.; Espinoza-Andaluz, M. Evaluation of geometric tortuosity for 3D digitally generated porous media considering the pore size distribution and the A-star algorithm. *Sci. Rep.* **2022**, *12*, 19463.
(35) Armstrong, R. T.; Lanetc, Z.; Mostaghimi, P.; Zhuravljov, A.; Herring, A.; Robins, V. Correspondence of max-flow to the absolute permeability of porous systems. *Physical Review Fluids* **2021**, *6*, 054003.
(36) Qin, C.-Z.; van Brummelen, H.; Hefny, M.; Zhao, J. Image-based modeling of spontaneous imbibition in porous media by a dynamic pore network model. *Advances in Water Resources* **2021**, *152*, 103932.
(37) Animation showing pore distribution in nano-porous carbon in 2D. Credit: Nowier Rawan; Ohio University. http://people.ohio.edu/drabold/animations/NPC_2d_PSD.mp4 (accessed 2023-02-20).
(38) Soler, J. M.; Artacho, E.; Gale, J. D.; García, A.; Junquera, J.; Ordejón, P.; Sánchez-Portal, D. The SIESTA method for *ab initio* materials simulation. *J. Phys.: Condens. Matter* **2002**, *14*, 2745−2779.
(39) Ceperley, D. M.; Alder, B. J. Ground state of the electron gas by a stochastic method. *Physical review letters* **1980**, *45*, 566.
(40) Perdew, J. P.; Zunger, A. Self-interaction correction to density-functional approximations for many-electron systems. *Phys. Rev. B* **1981**, *23*, 5048−5079.
(41) Perdew, J. P.; Zunger, A. Self-interaction correction to density-functional approximations for many-electron systems. *Phys. Rev. B* **1981**, *23*, 5048.
(42) López, M. J.; Cabria, I.; Alonso, J. A. Simulated porosity and electronic structure of nanoporous carbons. *J. Chem. Phys.* **2011**, *135*, 104706.
(43) Subedi, K. N.; Prasai, K.; Drabold, D. A. Space-Projected Conductivity and Spectral Properties of the Conduction Matrix. *physica status solidi (b)* **2021**, *258*, 2000438.
(44) Sankey, O. F.; Niklewski, D. J.; Drabold, D.; Dow, J. D. Molecular-dynamics determination of electronic and vibrational spectra, and equilibrium structures of small Si clusters. *Phys. Rev. B* **1990**, *41*, 12750.
(45) Harris, F. J. On the use of windows for harmonic analysis with the discrete Fourier transform. *Proceedings of the IEEE* **1978**, *66*, 51−83.
(46) Romero, C.; Valladares, A. A.; Valladares, R.; Valladares, A. Electronic and vibrational densities of states of ab initio generated nanoporous carbons. *J. Non-Cryst. Solids* **2013**, *362*, 14−19.
(47) Bhattarai, B.; Drabold, D. Amorphous carbon at low densities: An ab initio study. *Carbon* **2017**, *115*, 532−538.
(48) Bhattarai, B.; Pandey, A.; Drabold, D. Evolution of amorphous carbon across densities: An inferential study. *Carbon* **2018**, *131*, 168−174.
(49) Al-Qasir, I. I.; Campbell, A. A.; Sala, G.; Lin, J. Y.; Cheng, Y.; Islam, F. F.; Abernathy, D. L.; Stone, M. B. Vacancy-driven variations in the phonon density of states of fast neutron irradiated nuclear graphite. *Carbon* **2020**, *168*, 42−54.
(50) Surblys, D.; Matsubara, H.; Kikugawa, G.; Ohara, T. Methodology and meaning of computing heat flux via atomic stress in systems with constraint dynamics. *J. Appl. Phys.* **2021**, *130*, 215104.
(51) Surblys, D.; Matsubara, H.; Kikugawa, G.; Ohara, T. Application of atomic stress to compute heat flux via molecular dynamics for systems with many-body interactions. *Phys. Rev. E* **2019**, *99*, 051301.
(52) Green, M. S. Markoff Random Processes and the Statistical Mechanics of Time-Dependent Phenomena. II. Irreversible Processes in Fluids. *J. Chem. Phys.* **1954**, *22*, 398−413.
(53) Kubo, R.; Yokota, M.; Nakajima, S. Statistical-Mechanical Theory of Irreversible Processes. II. Response to Thermal Disturbance. *J. Phys. Soc. Jpn.* **1957**, *12*, 1203−1211.
(54) Nosé, S. A molecular dynamics method for simulations in the canonical ensemble. *Mol. Phys.* **1984**, *52*, 255−268.
(55) Hoover, W. G. Canonical dynamics: Equilibrium phase-space distributions. *Phys. Rev. A* **1985**, *31*, 1695−1697.
(56) Coquil, T.; Fang, J.; Pilon, L. Molecular dynamics study of the thermal conductivity of amorphous nanoporous silica. *Int. J. Heat Mass Transfer* **2011**, *54*, 4540−4548.
(57) Mi, X.; Shi, Y. Elastic Properties of Mimetically Synthesized Model Nanoporous Carbon. *MRS Proceedings* **2009**, *1224*, 1010.
(58) Caro, M. A.; Aarva, A.; Deringer, V. L.; Csányi, G.; Laurila, T. Reactivity of amorphous carbon surfaces: rationalizing the role of structural motifs in functionalization using machine learning. *Chem. Mater.* **2018**, *30*, 7446−7455.
(59) Olson, R., III (CONSOL Innovations), Private Communication- Discussion on preferential adsorption of water in the nanoporous reticulated vitreous carbon form made from furfuryl alcohol or phenolic resin precursors, 2023. See ref 60 for associated research.
(60) Haack, D.; Olson III, R. Processing, Microstructure and Properties of Reticulated Vitreous Carbon Foam Manufactured via the Sponge Replication Technique. *Advances in Bioceramics and Porous Ceramics V* **2012**, 175−185.
(61) Hoffmann, D. T.; Dietrich, J.; Mändl, S.; Zink, M.; Mayr, S. G. Nanoporous Morphogenesis in Amorphous Carbon Layers: Experiments and Modeling on Energetic Ion Induced Self-Organization. *Advanced Theory and Simulations* **2021**, *4*, 2100093.
(62) Mejía-Mendoza, L.; Valdez-Gonzalez, M.; Muñiz, J.; Santiago, U.; Cuentas-Gallegos, A.; Robles, M. A theoretical approach to the nanoporous phase diagram of carbon. *Carbon* **2017**, *120*, 233−243.
(63) Kresse, G.; Furthmüller, J. Efficient iterative schemes for ab initio total-energy calculations using a plane-wave basis set. *Phys. Rev. B* **1996**, *54*, 11169−11186.
(64) Perdew, J. P.; Burke, K.; Ernzerhof, M. Generalized Gradient Approximation Made Simple. *Phys. Rev. Lett.* **1996**, *77*, 3865−3868.

https://doi.org/10.1021/acs.jctc.3c00394
J. Chem. Theory Comput. XXXX, XXX, XXX−XXX